Application of a particle simulation to modeling commutation in a linear thyratron[a)]

Mark J. Kushner[b)]
Spectra Technology, Inc., 2755 Northup Way, Bellevue, Washington 98004

(Received 4 August 1986; accepted for publication 17 December 1986)

Commutation is the period during which a thyratron makes the transition between an open state and a conducting state. During commutation the voltage across the thyratron decreases from the holdoff voltage to the conduction value; 10's of kV to < 100 V. The time for commutation, as measured by the anode voltage fall time, is usually 10–100 ns, a value which depends on the holdoff voltage, internal gas pressure, and grid geometry. In this paper, a model for commutation in a thyratron is described and its results are compared to experiment for a thyratron having a linear geometry. The model uses a Monte Carlo particle simulation for electrons and a continuum fluid representation for ions. A particle multiplication and renormalization scheme is used in the model to simulate electron avalanche so that only a moderate number of particles (4000–12000) need to be used. A modified null cross-section technique is used to account for large changes in the density of electron collision partners as a function of position or time. A model for the external circuit enables simulation of current and voltage. Results from the model for these quantities agree well with experiment, and indicate that commutation occurs in two stages. A survey study contrasts the tradeoff between high-voltage holdoff and switching speed.

I. INTRODUCTION

Thyratrons are multigrid electrical plasma switches that operate on the near side of Paschen's curve.[1,2] High-voltage holdoff (typically $\leqslant 45$ kV per gap) is obtained by operating with small $P \times D$ (gas pressure $\times$ electrode separation) products. Typical gas pressures and electrode separations are < 1.0 Torr and < 1.0 cm, respectively. Thyratrons are the electrical gas switch of choice for high repetition rate (> 1 kHz), moderate voltage ($\leqslant 45$ kV), and moderate current (< 5 kA, $dI/dt < 10^{10}$ A s^{-1}) applications. When higher voltages, larger currents, and larger dI/dt are required, spark or rail-gap switches are usually used.[3] The switching cycle of a thyratron can be divided into three regimes: holdoff, commutation, and conduction. During holdoff the thyratron passes no current and the circuit is open, while during conduction the circuit is closed and the thyratron is a negligible resistance compared to the load ($\ll 1\ \Omega$). During conduction, the normalized electric field within the thyratron is low (< 50 Td, 1 Td $= 1.0 \times 10^{-17}$ V cm^2) and the fractional ionization can be large ($\leqslant 0.1$). Characteristics of thyratrons during conduction have been studied and are well understood.[1,2,4–8] Commutation is the period during which electron avalanche of the gas in the thyratron occurs resulting in a conducting state. During commutation the voltage across the thyratron decreases by many orders of magnitude from the holdoff voltage to the conduction value (10's of kV to < 100 V). The time for commutation, as measured by the anode voltage fall time, is usually 10–100 ns, a value which depends on the holdoff voltage, internal gas pressure, and grid geometry.

Since commutation in a thyratron is a transient process having a parameter space which spans many orders of magnitude, it has proved to be difficult to model. The plasma changes from being weakly ionized to being locally highly ionized; and, under certain conditions, spatial inhomogenities in the fractional ionization and local electric field have dimensions which are commensurate with the mean-free path of electrons. Electrode separations also have these dimensions. In this paper, a model using a particle simulation for electron transport is described, and is applied to modeling commutation in a thyratron having a linear geometry. A particle simulation was chosen to model commutation in a thyratron because of the difficulty in using a continuum model in complex and arbitrary geometries, under conditions where the range of electron energies is large (0.1 eV to > 1 keV), and where the fractional ionization varies widely (10^{-10} to 0.01). The model has successfully simulated current and voltage characteristics during commutation for a linear thyratron operating in helium at voltages up to 75 kV. The model has been less successful at simulating thyratron characteristics during conduction; continuum models are more appropriate for that phase of operation.[4]

The model is a 2 1/2-dimensional time-dependent simulation of an electron avalanche in a multigrid gas discharge switch. The geometry that is modeled is user defined, and can consist of a selection of metallic or dielectric materials. Electron transport is modeled using a particle simulation and collisions with the gas (e.g., elastic, excitation, ionization) are simulated using Monte Carlo techniques. Heavy particle transport (i.e., ions, excited states) is modeled using conventional continuum partial differential equations whose source term is obtained from electron collisions in the particle simulation. The local electric potential is obtained by solution of a modified Poisson's equation. Models for the

[a)] Work supported by Air Force Systems Command (Wright Patterson Air Force Base) Contract No. F33615-84-C-2474.

[b)] Present address: University of Illinois, Department of Electrical and Computer Engineering, Gaseous Electronics Laboratory, 607 E. Healey, Champaign, IL 61820.

 0021-8979/87/082784-11$02.40

electric circuit for each grid or electrode are included in the simulation so that current and voltage characteristics during commutation can be generated.

The physical device that provides the experimental data for validation of this model is thyratron using a linear geometry. This device will be briefly described in Sec. II. The model, called LINTHY, will be presented in Sec. III, and results from the model will be compared to experiment in Sec. IV. Scaling laws for switching speed and high-voltage holdoff generated with results from the model are discussed in Sec. V and concluding remarks are in Sec. VI.

II. THE LINEAR THYRATRON

Thyratrons are conventionally built using a cylindrical geometry for the cathode and anode structures. Scaling cylindrical thyratrons to higher currents by increasing the diameter of the cathode has had limited success because of the inability to uniformly utilize the entire cathode surface, and because of the increase in inductance obtained with such scaling. In an effort to increase the current and dI/dt of thyratrons while avoiding the problems traditionally associated with scaling cylindrical thyratrons, a thyratron using a linear geometry has been built. Details of the construction and performance of this thyratron can be found in Refs. 9 and 10. The linear geometry is conceptually scalable to large currents by lengthening the thyratron in the axial dimension while not changing the characteristic gap dimensions or the distance between any spot on the cathode and the control grid slot, the critical dimensions which determine the switching properties.

Schematics of the linear thyratron in two configurations are shown in Fig. 1. The thyratron is a tetrode, having both auxiliary and control grids. The slotted dispenser cathode has dimensions 3×10 cm. Voltage is held off between the control grid and anode, while a dc simmer current (a few mA cm^{-2} of cathode area) is sustained between the cathode and the auxiliary grid. Switching is obtained by simultaneously pulsing the auxiliary and control grids, collapsing the voltage between the cathode and control grid. The anode potential then penetrates through the control grid slot, drawing plasma to the anode and closing the switch. The thyratron is typically operated in either hydrogen or helium. The results discussed here are for operation in helium. Uniform and simultaneous discharge coverage over the entire area of the cathode is obtained by operating with the dc simmer current.

The prototype device [Fig. 1(a)] has separately switched 25 kV, 10 kA, and a maximum dI/dt of 1.3×10^{11} A s^{-1}. Typical operation, though, was with an anode voltage of 8–10 kV. The modified high-voltage linear thyratron [Fig. 1(b)] has switched 95 kV in both H_2 and He with a dI/dt of 3×10^{10} A s^{-1}.

III. DESCRIPTION OF THE MODEL

LINTHY is a 2 1/2-dimensional electron particle and ion fluid model for simulation of commutation in a thyratron. The results discussed here are for a linear thyratron operating in helium. Collisions in the electron particle simulation are computed using Monte Carlo methods. The change in local current density during commutation implies a change in electron density of 10^6–10^{14} cm^{-3}. To model commutation with Monte Carlo techniques using a finite number of particles, each particle must represent a large number of electrons. The number of electrons each particle

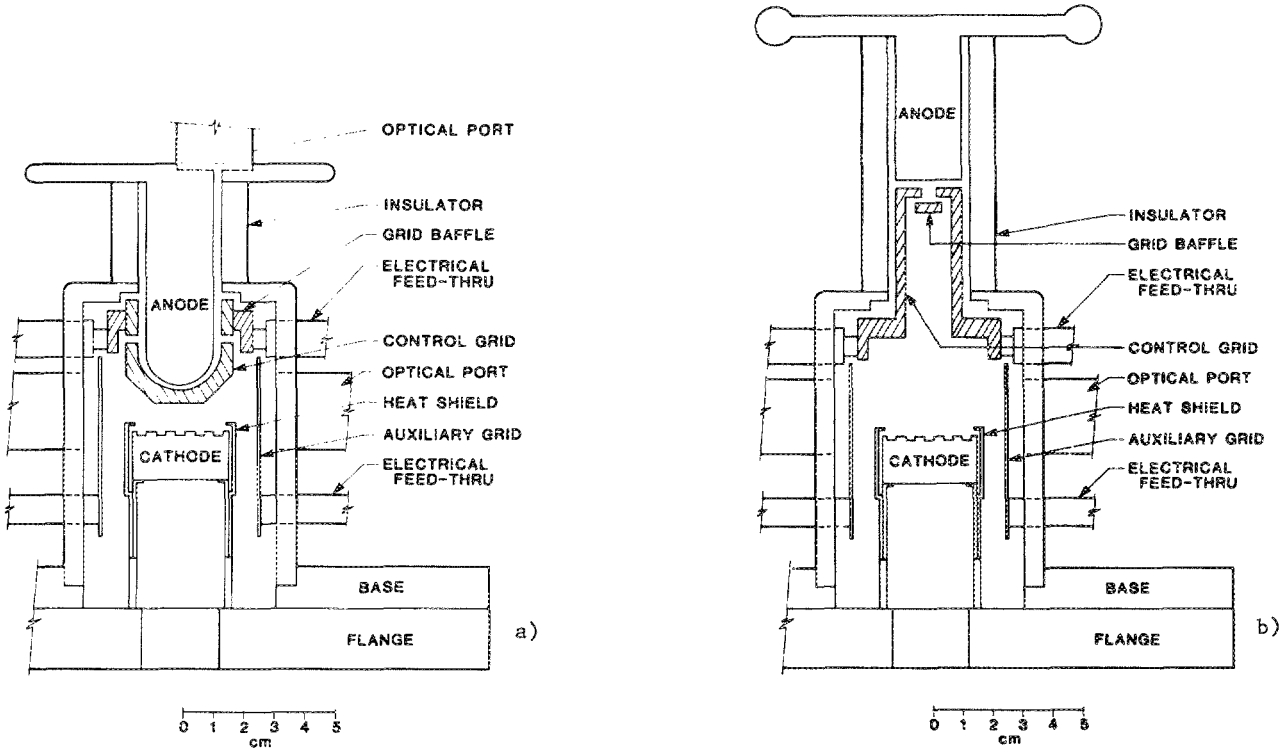

FIG. 1. Schematics of the prototype (left) and high-voltage (right) linear thyratrons. The slotted dispenser cathode is 3×10 cm. The gap between the control grid and anode is 2.5 mm. To trigger the thyratron, both the auxiliary and control grids are pulsed to a few kilovolts.

represents in the simulation is called its "weight" and the particles are called macroelectrons. When a macroelectron causes an ionization, an additional macroelectron is added to the simulation. Periodically the number of macroelectrons exceeds a specified maximum value. At that time, the number and weights of the electrons are renormalized in a manner similar to that used by Kline and Siambis.[11] The renormalization sequence is described below.

A. Renormalization of the macroparticles

The simulation begins with N_0 macroelectrons released from the cathode, each having a weight $W_0 = I/(eN_0\Delta t)$, where I is the instantaneous current and Δt is the length of time over which the N_0 electrons are released. Trajectories and collisions for the macroelectrons are computed using standard Monte Carlo techniques.[12] When an ionization occurs, another macroelectron is added to the simulation at the site of the ionization with a weight equal to the weight of the macroelectron having had the collision. (Recall that the weight of the particle refers to the number of electrons it represents and not its mass.) Simultaneously, macroelectrons are released from the cathode with a weight corresponding to the instantaneous current. If a macroelectron collides with a grid or electrode, its weight is summed to obtain current to that grid or electrode, and the macroelectron is removed from the simulation. At this time a table of material properties is consulted to determine whether secondary electron emission should occur. If so, a secondary macroelectron is released from the surface. When the total number of macroelectrons exceeds a preselected value, $N_{\max}$, the simulation is interrupted for renormalization. The total weight of the macroelectrons is summed. N_0 macroelectrons are then randomly selected and their weights are summed. The unselected macroelectrons are removed from the simulation, and the weights of the remaining macroelectrons are summed. To conserve total charge, the weights of the remaining macroelectrons are increased by the ratio of weights before and after reducing the number of macroelectrons. The simulation then proceeds with fewer macroelectrons, but each macroelectron represents more electrons. The normalization procedure is separately performed within different spatial regions of the thyratron to insure that the local charge density is not significantly perturbed. Since the renormalization process decreases the number of macroelectrons, the instantaneous random error is larger after renormalization. This is, of course, a tradeoff that must be made against using very large numbers of particles.

The number of macroelectrons used in the simulation fluctuates between N_0 and $N_{\max}$ (typically 4000 and 12000 particles respectively) with renormalization occurring approximately every 2–5 ns during commutation. The typical weight of a macroelectron at the start of commutation is 10^4. At the end of commutation (i.e., at the beginning of conduction), each macroelectron represents 10^9 electrons. The large weight of the macroelectrons at this time causes statistical fluctuations during the calculation which are unphysical. Simulation of conduction using this method in complex geometries is therefore difficult. The remedy is to use more particles, which may be prohibitive, or to use continuum methods to model conduction.[2,8] A typical case using this model, simulating 50–150 ns of commutation, requires 8–16 h of CPU time on a VAX-11/780 computer.

B. Modified null cross-section technique

During Monte Carlo simulations of electron collisions in gas discharges, it is convenient for all electrons to appear to have the same collision frequency so that the mean time between "collisions" is effectively independent of electron energy. This is accomplished by use of a null cross section.[12] In using the null cross-section technique, the maximum electron collision frequency for the energy range of interest, $\nu_{\max}$, is determined. At each electron energy, a fictitious cross section, called the null cross section, is calculated so that when this cross section is added to the real collision cross sections, the resulting collision frequency is equal to $\nu_{\max}$. During the simulation, a collision is said to occur during a time Δt if for a random number r_1 $(0 < r_1 < 1)$, $\Delta t \geqslant -\ln(r_1)/\nu_{\max}$. If this inequality holds another random number r_2 is selected. A real collision is said to occur if $r_2 \leqslant \nu_a/\nu_{\max}$, where ν_a is the actual collision frequency. If the collision is not real (i.e., a null collision) the electron proceeds unhindered.

During an electron avalanche, the relative densities of species with which the electrons collide can change significantly as a function of either position or time. The densities change as a result of electron impact excitation and ionization of the gas. The maximum electron collision frequency, and the number and types of collisions, also change as a function of position and time. The collision frequency of an electron traversing regions having different densities of collision partners therefore will change in a manner not accounted for in the initial calculation of $\nu_{\max}$. To easily account for these changes, a modified null cross-section technique was developed. In using this technique, cross sections for all *anticipated* processes that may be important during the simulation (e.g., electron-electron collisions, electron-ion collisions, superelastic collisions with excited states) are included in the initial computation of the individual collision frequencies for each process, and for the maximum collision frequency $\nu_{\max}$. In doing so, one must estimate the maximum possible density that each of the collision partners may have during the time of interest. The collision frequency for each energy then consists of the sum of the collision frequencies with all species and all processes as calculated with the maximum anticipated density of the species, $\nu_a = \Sigma\nu_a^j$; and a collision frequency that is always null, ν_{null} (as described above) so that $\nu_{\max} = \nu_{\text{null}} + \nu_a$. In order to minimize the fraction of the cross section that is null, the energy range of interest was divided into 4–5 subranges. A separate $\nu_{\max}$ was computed for each subrange. In this way, the large ν_{null} that is necessary to account for Coulomb collisions at low energy at the beginning of the calculation is not carried to high energies where the Coulomb cross section is small. We attempted to have the working null space represent no more than half the collision frequency.

The sequence of operations that is followed to determine whether a collision of type j occurs is as follows, where r_i is a random number $(0 < r_i < 1)$. A collision occurs during Δt if

$\Delta t \geqslant -\ln(r_1)/\nu_{\max}$; a collision occurs that could be real if $r_2 \leqslant \nu_a/\nu_{\max}$; a collision of type j occurs if $\nu_a^{j-1}/\nu_{\max} < r_3 \leqslant \nu_a^j/\nu_{\max}$; and a real collision occurs if $r_4 \leqslant N_j(x,y,t)/N_j^{\max}$. $N_j(x,y,t)$ is the instantaneous density of the collision partner for process j, and $N_j^{\max}$ is its maximum anticipated value. (By appropriate scaling a single random number can be used in place of r_1–r_4.) Using the modified null cross-section technique, large changes in the density of collision partners can be easily modeled, particularly when between collisions, the electron traverses regions having a significantly different density of collision partners.

C. Electron collision processes

Four states of helium were included in the simulation; the ground state, a single excited state, and singly and doubly ionized atoms. The following electron impact excitation reactions were used:

Electron-neutral elastic scattering,

$$e + M(*) \rightarrow M(*) + e;$$

Electron-ion elastic scattering,

$$e + M^+ \rightarrow M^+ + e;$$

Electron-electron scattering,

$$e + e_{\text{ave}} \rightarrow e_{\text{ave}} + e;$$

Electronic excitation and superelastic relaxation,

$$e + M \rightleftarrows M^* + e;$$

Ionization,

$$e + M \rightarrow M^+ + e + e_s;$$

Double ionization,

$$e + M \rightarrow M^{2+} + e + 2e_s;$$

Excited-state ionization,

$$e + M^* \rightarrow M^+ + e + e_s;$$

Radiative recombination,

$$e + M^+ \rightarrow M^*, \quad e + M^{++} \rightarrow M^+;$$

Collisional radiative recombination,

$$2e + M^+ \rightarrow M^* + e, \quad 2e + M^{++} \rightarrow M^+ + e.$$

In the reactions above, M is the ground state of the noble gas and M^* is the excited state. M^+ and M^{2+} are the single and doubly ionized atom, respectively. The subscripted electron e_s denotes the secondary electron in an ionization. The "average" electron is denoted by e_{ave} and will be discussed below. Including collisions between charged particles is particularly important because the plasma can become highly ionized ($\approx 10^{-3}$–10^{-2}) near the control grid slot. At such times, the current density is locally constrained by electron-ion collisions.

Neutral elastic scattering cross sections for helium were obtained from the compilation by Hayashi[13]; and for the excited state from Fon *et al.*[14] and Donaldson *et al.*[15] Cross sections for single and double ionization of ground state atoms were obtained from Rapp and Englander-Golden,[16] and Stephens *et al.*,[17] respectively. The secondary electron distribution was obtained from Green and Sawada.[18] The semi-empirical cross sections of Vriens were used for ionization of the excited state.[19]

The cross sections for elastic scattering from charged species, both electrons and ions, were obtained in analytic form from Mitchner and Kruger,[20]

$$\sigma(\epsilon,n_e,T_e) = 4\pi b_0^2 \ln(1 + \lambda^2/b_0^2),$$

where ϵ is the electron energy, λ is the Debye length

$$\lambda^2 = \epsilon_0 k T_e/n_e e^2$$

and

$$b_0 = [e^2/(8\pi\epsilon_0)]/\epsilon.$$

To evaluate these cross sections and collision frequencies, the electron temperature (T_e), electron density (n_e), and ion density are required. The ion density is obtained from solution of the heavy particle conservation equations discussed below. The local electron density is obtained by periodically summing and averaging a sequence of "snapshots" of the location of the macroelectrons at preset intervals. An effective electron temperature is computed in this same manner by weighting the sum by the energy of each macroelectron and setting $T_e(x,y,t) = 2\bar{\epsilon}(x,y,t)/3\text{k}$, where $\bar{\epsilon}$ is the local average electron energy. The average electrons in the reactions listed above are then assigned values of n_e and T_e, and the most recently summed values for electron density and temperature are then used to calculate the cross section for electron-electron (ee) and electron-ion (eI) collisions. At the start of the simulation, at the onset of commutation, the electron and ion densities are negligible. A range of n_e, n_i, and T_e must therefore be estimated before the simulation in order to provide sufficient working null space in the ee and eI collision frequencies to account for collisions when the plasma is significantly ionized. When an ee collision occurs, the collision partner is assumed to be an average electron. The actual collision partner is an electron with a velocity randomly selected from a Maxwellian distribution having temperature T_e. In this manner, the electron distribution, in the absence of other collisions, relaxes to a Maxwellian.

The azimuthal scattering angle for electron-heavy particle collisions was assumed to be isotropic. The probability for scattering through the polar angle θ was assumed to have the form

$$p(\theta) \propto \cos^m(\theta/2). \tag{1}$$

For $m = 0$, the scattering is isotropic; for $m \gg 1$, the scattering is dominantly forward. The randomly distributed scattering angle, θ_s is obtained from $p(\theta)$ by normalizing the differential scattering probability to unity for scattering in the range $0 \leqslant \theta_s \leqslant \pi$, and inverting the integral.[21]

$$\theta_s = 2\cos^{-1}[(1-r)^{1/(m+2)}]. \tag{2}$$

When experimental data were available for the differential cross section, the value of m was chosen to approximate the experimental data by making m dependent on energy. If no experimental data were available, a value of $m \approx 3$ was typically used to allow some forward scattering, as is typical at energies of greater than a few eV. At energies below the first inelastic threshold, one can deduce a value of m by noting that

$$\sigma_{MT}/\sigma_{EL} = 2\{1 - [(m+2)/(m+4)]\}, \tag{3}$$

where σ_{MT} is the momentum transfer cross section and σ_{EL} is the elastic cross section. The choice of cross sections was validated by using the simulation to compute electron transport coefficients and comparing the results to experimental swarm data.[22]

D. Heavy particle transport

The densities of heavy particles (neutrals, excited states, and ions) were obtained by solution of continuum transport equations. The conservation equations used for heavy particle type j having number density N_j, mass M_j, and charge Z_j are

Momentum:

$$\frac{\partial(\mathbf{u}_j N_j)}{\partial t} = -\nabla\cdot\mathbf{u}_j\mathbf{u}_j N_j + \frac{Z_j e \mathbf{E} N_j}{M_j} - N_j \mathbf{u}_j \nu_{CE}, \quad (4)$$

Continuity:

$$\frac{\partial N_j}{\partial t} = -\nabla\cdot\mathbf{u}_j N_j + S_j(x,y,t) + D_j\nabla^2 N_j - \frac{N_j}{\tau}, \quad (5)$$

where $\mathbf{u}_j$ is the velocity of particle type j, $\mathbf{E}$ is the local electric field, D_j is the diffusion constant, and $S_j(x,y,t)$ is the source function for electron impact collisions exciting species j. ν_{CE} is the collision frequency for charge exchange, and τ is an effective radiative lifetime. In modeling a mono-atomic gas, charge exchange is resonant and therefore appears only as a term for momentum damping.

Cross sections for resonant charge exchange collisions for He^+ were obtained as a function of energy from Duman and Smirnov.[23] Diffusion constants for ions were derived from the compilation of Ellis, Pai, and McDaniel.[24] The source function $S_j(x,y,t)$ is obtained directly from the electron particle simulation by summing the collisions of macroelectrons over a preselected time (typically 1–2 ns) occurring in a volume of one computational cell centered on (x,y). Equations (4) and (5) were solved using a second-order donor cell integration scheme.

The boundary conditions for the momentum and continuity equations are that the ion momentum and density are zero at all solid boundaries. The flux of ions colliding with the cathode is summed over a preselected time (typically 1–2 ns) and secondary electrons are released from the cathode as specified by the flux of ions and the secondary emission coefficient. Secondary electron emission by both electron and ions impacting on grids was included using a secondary emission coefficient of 0.1. We saw little change in the results of the simulation during commutation when including secondary emission from surfaces other than the cathode. This is particularly true of secondary electron emission from the anode because the large electric fields at the site of emission prevents the secondary electron from penetrating back into the plasma.

E. Electric potential

The local electric potential ϕ, and by differentiation the electric field, within the plasma is obtained by solution of a modified Poisson's equation

$$\nabla\cdot\epsilon\nabla\phi = \gamma\rho/\epsilon_0 = \gamma e(n_I - n_e)/\epsilon_0, \quad (6)$$

where ϵ is the local dielectric constant, ρ is the local charge density, and γ is a factor to be discussed below. For insulators the actual value of ϵ was used; otherwise we set $\epsilon = 1$. The electron density is obtained by summing the local density of macroparticles during a series of "snapshots" of the particle distribution. The ion density is obtained from the solution of the ion continuity equation. The boundary conditions at the surfaces of the cathode, auxiliary grid, control grid, and anode are given by the values of the electric potential of those surfaces obtained from the circuit equations (see below). Equation (6) was solved using the method of successive over relaxation (SOR) using a 9-point numerical molecule.[25] The potential distribution in the simulation was typically updated every 1–3 ns.

Due to the statistical nature of the Monte Carlo method when using a small number of particles, there are fluctuations in the charge density which are unphysical. The fluctuations in charge density result from ionization collisions which are infrequent compared to nonionizing elastic collisions. This aspect of the simulation for a partially ionized gas during commutation differs from particle simulations of fully ionized plasmas[26] where all collisions are elastic (i.e., nonionizing) and therefore do not directly contribute to the local charge density. These fluctuations are reduced by numerically smoothing the computed charge density using a 9-point numerical molecule.[25] Further smoothing of ρ, though, was found to be necessary. This smoothing is represented by the factor γ in Eq. (6). The smoothing consisted of clamping fluctuations in the charge density to, at most, a few times the local average. The smoothing factor is determined locally and therefore is a function of both position and time.

An example of the electric potential computed in the fashion described above for the high-voltage linear thyratron is shown in Fig. 2. Note the nearly equipotential region in front of the baffle and the penetration of potential lines from the anode through the control grid slot. The penetration of the anode potential through the slot is an important consideration in high voltage holdoff and switching speed, a topic discussed in Sec. V.

F. Circuit model

A thyratron using a tetrode geometry is connected to three electrical circuits: one each to drive the auxiliary and

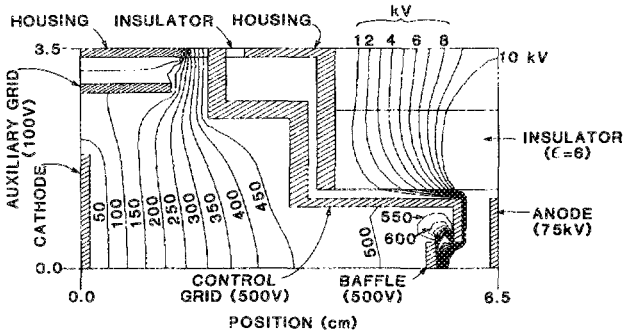

FIG. 2. Electrical potentials for the high-voltage linear thyratron. The cathode and stainless-steel housing are at ground potential, the auxiliary grid is at 100 V, the control grid is at 500 V, and the anode is charged to 75 kV. The insulator has a dielectric constant of 6. Note the nearly equipotential region within the bounds of the control grid, and note the penetration of the anode potential through the control grid slot.

control grids, and the energy storage circuit, which is the circuit being switched by the thyratron. In conventional discharge models, the plasma is treated as a time-dependent resistor within the circuit having resistance $R = L/(\sigma A)$, where σ is the conductivity of the plasma, L is the series length of the plasma, and A is its cross-sectional area. This definition of resistance is not easily applied to a thyratron because there are no unambiguous definitions of σ, L, or A. As a result, different methods of computing the resistance of the plasma as a circuit element must be used. In this simulation, the thyratron was represented as a resistive current source and a "conventional" resistor.

When treating the plasma as a current source, during a time interval Δt the weights of the macroelectrons collected by a particular grid or electrode are summed. The current flowing through, for example, the control grid circuit, is then $I_{CG} = (\Sigma e W_i)/\Delta t$, where the sum is over all macroelectrons collected by the control grid. Given that this current is flowing through the control grid circuit, the time rate of change in current can be computed from the previous value of current, and the change in voltage across each of the circuit elements can be computed. For example, the voltage drop across an inductor is $\Delta V = L(I_{CG}^{\text{new}} - I_{CG}^{\text{old}})/\Delta t$. With these changes in voltage, the potential of the control grid can be revised using Kircchoff's law. The current through each of the three discharge circuits is summed to yield the total cathode current, I_C. This value is then used to specify the weight of the macroelectrons released from the cathode during the next time interval, $W = I_C \Delta t/(eN_0)$, where N_0 is the number of macroelectrons released.

When treating the plasma as a "conventional" resistor, one or more parallel current paths, from cathode to anode, are specified. During successive time intervals Δt, the electron density and electron collisions along path s_i are summed and averaged, yielding $n_e^i(s)$ and $\nu_c^i(s)$, respectively. The resistance for current flow along the path is then computed from the integral

$$R_i = \int_{s_i} \frac{m_e \nu_c^i(s)}{e^2 n_e^i(s) A_i(s)}\, ds, \tag{7}$$

where $A_i(s)$ is the width of the path. The resistance of the plasma in the thyratron is then obtained by $R = (\Sigma 1/R_i)^{-1}$ where the sum is over the number of specified parallel current paths. Using this method requires at least one iteration of the calculation to confirm that the chosen current paths are indeed the most probable. Usually only a few iterations are required for each new geometry to converge on the most likely current paths. For a particular geometry, once the paths were determined they were not revised as conditions, such as anode voltage, were changed.

IV. COMPARISON OF PLASMA SIMULATION RESULTS WITH EXPERIMENT

Validation of the plasma simulation code LINTHY was performed by comparing results from the model with experimental data for voltage and current during commutation. This comparison is shown in Fig. 3(a) for the prototype geometry in Fig. 1(a). The anode holdoff voltage is 8 kV and the gas pressure is 1.2 Torr of helium. The agreement is qualitatively good. The computed resistance of the thyratron is shown in Fig. 3(b). Three separate trials for the same conditions are plotted in Fig. 3(b) showing the reproducibility of the Monte Carlo method. Commutation for these conditions appears to progress through two stages, with the transition occurring at $\approx$30 ns. The $1/e$ time constants for decrease in thyratron resistance for the two stages are 9 and 17 ns, respectively. The first stage we call "runaway" and the second we call "collisional." For times less than 30 ns, the grid voltages are high (many hundreds of volts), and the average E/N is hundreds to a few thousand Td. Electrons are rapidly accelerated above a few hundred eV to an energy range where the electron mean free path is greater than typical grid separations ($\gamma > d$). Electron transport is nearly ballistic. The thyratron resistance decreases inversely proportional to the increase in electron density and depends little on the average electron energy. When grid potentials fall below a few hundred volts and the average electron energy falls below tens of eV, the momentum transfer cross section increases to a sufficiently large value that $\lambda < d$. At this time, the electron collision frequency increases, the electrons more resemble a swarm and the thyratron resistance depends both on electron density and average energy.

The computed electron density for the conditions of Fig. 3 is shown in Fig. 4 for a $t = 15$ ns. The anode potential is 3.62 kV, the control grid voltage is 150 V, and the auxiliary grid voltage is 100 V. The distribution of electrons is quite nonuniform. A large density of electrons occurs near the

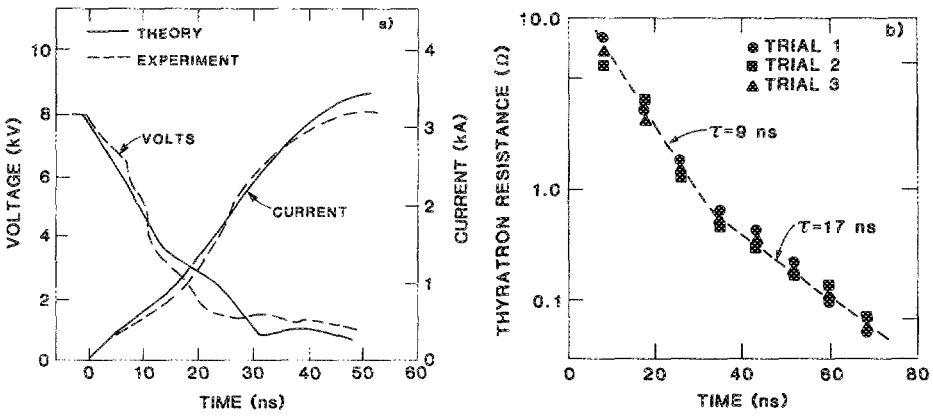

FIG. 3. Voltage, current, and thyratron resistance for the prototype thyratron. (a) Experimental and theoretical results, and (b) theoretical results for thyratron resistance. Three trials are plotted showing the reproducibility of the calculation. The τ is the time constant for decrease in thyratron resistance.

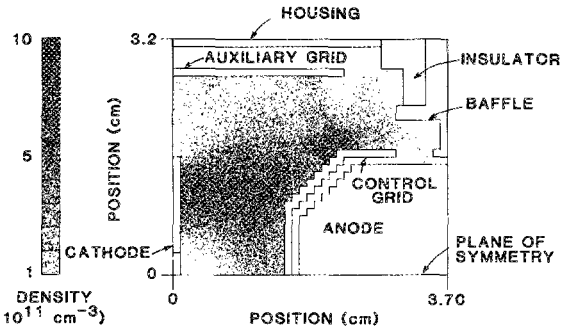

FIG. 4. Electron density at $t = 15$ ns for the conditions of Fig. 3 and the prototype geometry in Fig. 1. The electron density is represented by the density of dots, as normalized by the scale at left. These results are symmetric across the plane of the lower axis in the figure.

cathode, in the vicinity of the vertex of the control grid, and near the slot and baffle. The last two locations are regions of relatively high space charge and high potential due, in part, to the penetration of potential lines through the control grid slot after the breakdown of the cathode-grid space.

The volume averaged electron distribution function (EDF) at different times during commutation appears in Fig. 5 for the conditions of Fig. 3. Early during the discharge pulse when both the control grid and anode voltages are high, the EDF extends to well over 1 keV. The resistance of the thyratron is in the "runaway" stage at this time. As voltage collapses first between the control grid and cathode, and then between the anode and control grid, the EDF also collapses to lower energies. After 50–60 ns, the EDF at lower energy resembles a Maxwellian (see the inset in Fig. 5) and the resistance of the thyratron is in the "collisional" stage. The straight line in the plot of the EDF for $t = 55$ ns is a Maxwellian EDF having the equivalent electron temperature (13 eV). Note that the actual EDF has both an excess of low-energy electrons and a high-energy tail. This form of the distribution function results from the high average degree of ionization in the cathode-control grid region ($\geqslant 10^{-4}$). The large component of the distribution function near zero energy is due to the thermal electrons only recently emitted from the cathode. The high-energy tail to the distribution function results from electrons accelerated by the anode potential penetrating through the control grid slot.

The spatial distribution of electron energies for $t = 15$ ns is shown in Fig. 6. There are two regions where the density of electrons in the lowest energy group (0–30 eV) is high; near the cathode and in the approach to the control grid slot. The low-energy electrons near the cathode are thermal electrons which have only recently beem emitted. The high density of thermal electrons near the control grid vertex and near the slot result from; emission or reflection of electrons from the control grid, a high rate of ionization resulting in a large density of low-energy secondary electrons, and a high density of ions which increase the electron collision frequency thereby reducing the rate of energy gain. The next group of electrons with higher energy (30–100 eV) represent those electrons accelerated from the cathode and electrons accelerated from the thermal group near the vertex and into the control grid slot. Finally, the highest densities of electrons in the third group (100–500 eV) are found in the control grid slot and near the control grid-anode gap where the electric potential is high. The current to the anode (i.e., electrons which traverse the control grid-anode gap) is due almost entirely to electrons attracted through the control grid slot by penetration of the anode potential through the slot. The

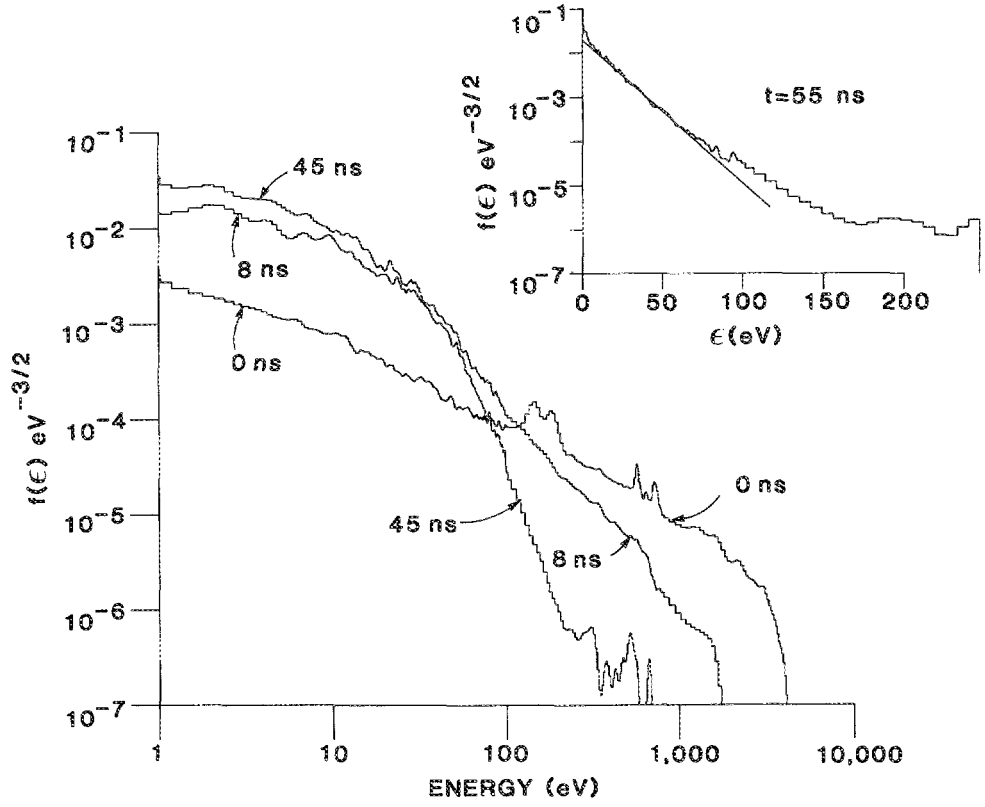

FIG. 5. Electron distribution function (EDF) for different times during commutation in helium. As voltage on the anode (initially 8 kV) and control grid (initially 3 kV) decrease, the EDF collapses to lower energy. The high-energy tail (best seen at 45 and 55 ns) results from electrons accelerated through the control grid slot. The straight line in the plot for 55 ns is a Maxwellian EDF having the same average energy ($T_e = 13$ eV).

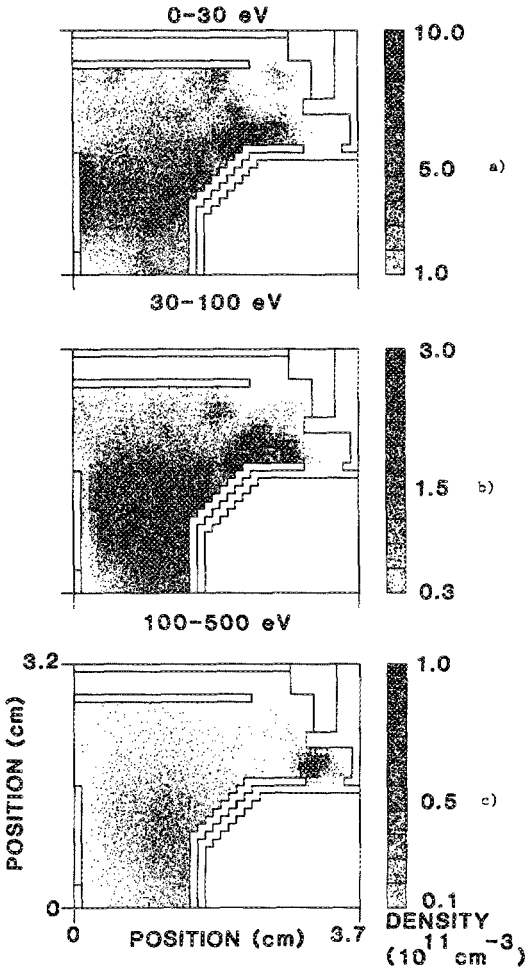

FIG. 6. Electron density in different energy ranges for the conditions of Fig. 3; 0–30 eV (top), 30–100 eV (middle), and 100–500 eV (bottom). The anode voltage is 3.62 kV and the control grid voltage is 150 V.

amount of ionization which occurs in the control grid-anode slot is minimal.

Experimental and predicted performance of the high-voltage linear thyratron [Fig. 1(b)] are shown in Fig. 7. On the left is a time sequence of snapshots of the electron density; on the right is voltage across the thyratron. The agreement for the voltage is good. A calculated value of jitter is obtained by running the simulation many times with different seeds for the random number generator. Jitter, in the simulation, appears to result from the nonoptimum configuration of the control grid. This configuration results in a nearly equipotential corridor through which the electron swarm must drift before reaching the control grid slot (see Fig. 2). When electrons drift into this volume from the region of comparatively high electric field between the cathode and control grid, their drift velocity slows. The slowly advancing and somewhat ragged leading edge of the swarm then determines when switching occurs. The anode delay time (the time between breakdown of the cathode-control grid space and collapse of the anode voltage) is therefore long and the jitter is large. The predicted jitter is smaller than the measured value. This discrepency indicates that a large portion of the jitter results from effects elsewhere in the circuit such as in the grid pulsers or charging circuit.

V. THE TRADEOFF BETWEEN HIGH-VOLTAGE HOLDOFF AND SWITCHING SPEED

Since thyratrons operate on the near side of the Paschen curve, high-voltage holdoff is obtained by operating with a small $P \times D$ product, where D is the separation between the control grid and the anode. Prefire can occur by exceeding the voltage specified by the $P \times D$ product, by field emission at sharp edges, or by leakage current from the cathode.

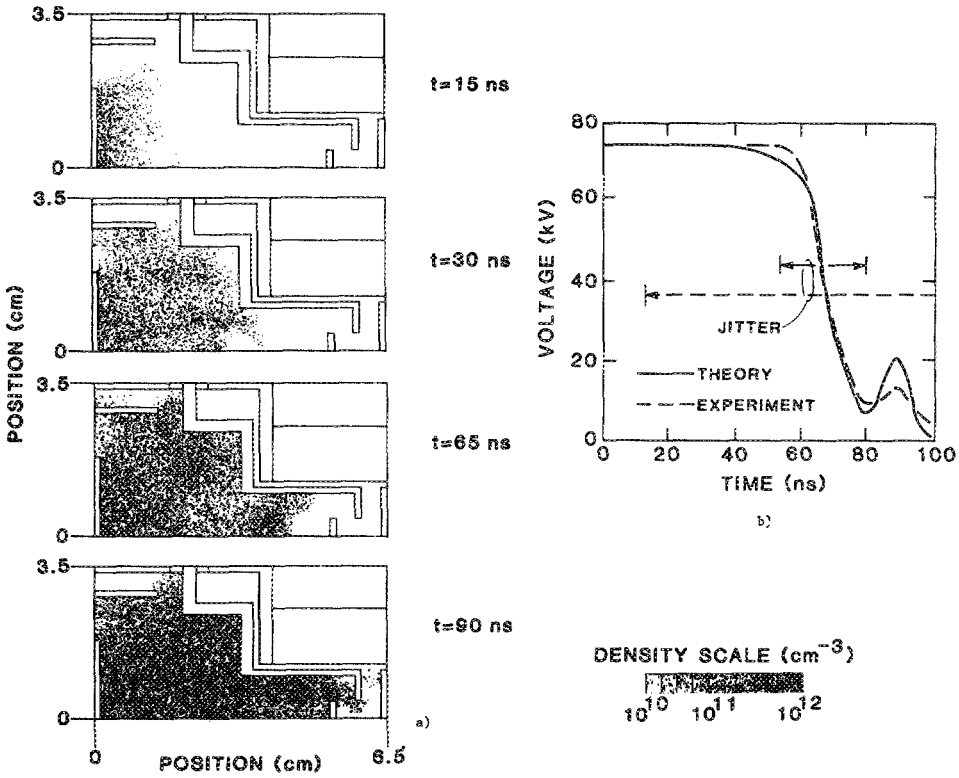

FIG. 7. Electron density (left); and voltage waveform (right) for the high-voltage linear thyratron. The electron densities in figures on the left are symmetric across the plane of the lower axis. See Fig. 2 for a key to the internal structure of high-voltage linear thyratron. The predicted voltage waveform agrees well with experiment however the computed jitter is too small.

Leakage current is a statistically occurring short between the cathode and anode during the holdoff phase resulting from a random flux of electrons originating near the cathode. These electrons originate from either using a hot thermionically emitting cathode, or a dc simmer current between the cathode and an auxiliary grid.

To prevent anode potential from attracting electrons into the control grid slot during holdoff, the control grid slot should be tightly baffled with a metallic shield electrically connected to the control grid. The shield, or baffle, prevents anode potential from penetrating into the cathode-control grid gap. A negative bias can be applied to the control grid to achieve the same goal. Both of these remedies, though, decrease the speed at which the thyratron can subsequently be switched. To minimize the switching time, the control grid slot should be loosely baffled to allow the anode potential to penetrate through the slot, and the control grid should be at the maximum possible voltage before switching. Both of these criteria are inconsistent with high-voltage holdoff. A tradeoff must therefore be performed between voltage holdoff (that is, preventing prefire) and switching speed.

To computationally examine the tradeoff between holdoff and switching speed, the thyratron geometry shown in Fig. 8 was used. The thyratron was modeled for operation with 250 μm of helium, using the linear geometry 10 cm in depth, and being symmetric across the lower plane of the figure. The parameter in this study is the separation between the control grid and the baffle, defined as the baffle offset D_b. The smaller this dimension, the more tightly the control grid slot is baffled.

We first calculated the value of the negative dc control grid bias, V_{dc}, necessary to insure that there is no leakage current to the anode. Leakage current was computed by "releasing" electrons from the cathode and determining the control grid bias for which no electrons released from the cathode are collected by the anode. The leakage current is defined as the fraction of the electrons released at the cathode that are collected by the anode. The value of V_{dc} required to insure there is no leakage current as a function of baffle offset and anode voltage is shown in Fig. 9 for three values of the anode voltage. Clearly, the more tightly baffled geometry requires a smaller value of V_{dc} to insure there is no leakage current to the anode. This trend results from the smaller value of electric potential penetrating through the control grid slot from the anode. At high holdoff voltages and as the baffle offset increases, the negative value of V_{dc} that is required to insure there is no leakage current increases at a higher rate than either the increase in voltage or D_b. This effect results from the higher value of the anode potential which penetrates through the control grid slot and which accesses, in energy, a larger fraction of the electron distribution in the cathode-control grid gap.

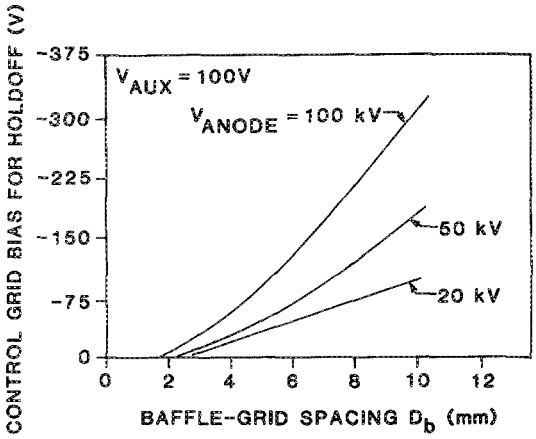

FIG. 9. Control grid bias required for no leakage current with the geometry of Fig. 8 for 0.25 Torr of helium. Results for three different anode potentials are shown.

LINTHY was then used to fully simulate commutation in the thyratron for the same conditions as above. An absolute switching time was calculated by determining the time required for the current to reach a specified value ΔI after pulsing the control grid. The absolute switching time for a holdoff voltage of 65 kV is plotted in Fig. 10 as a function of baffle offset for $\Delta I = 2$ kA. The switching time decreases with increasing gap size and increasing penetration of the anode potential. The actual points computed with LINTHY are plotted in this figure and show the statistical scatter of the method. The results shown in other figures are hand-drawn smoothed lines through a similar distribution of points.

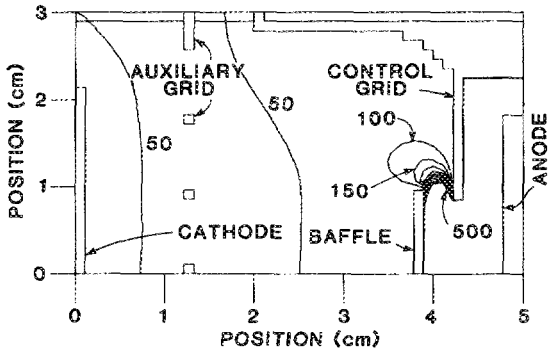

FIG. 8. Geometry used for the study of leakage current and switching speed. The electrical potential contours shown are for the cathode and control grid at ground potential, the auxiliary grid 100 V, and the anode at 100 kV.

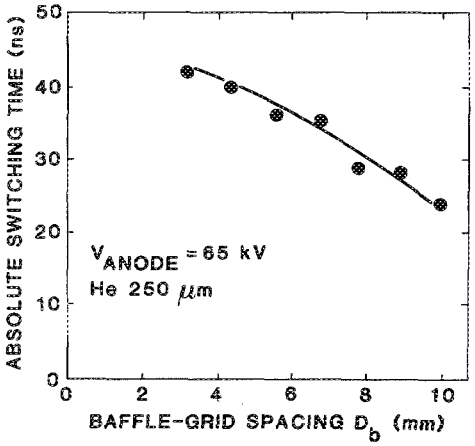

FIG. 10. The absolute switching time (time required for the current to rise to 2 kA) as a function of spacing between the control grid and baffle for the geometry of Fig. 8. The gas pressure is 0.25 Torr of helium and the anode is charged to 65 kV.

Since the rate of current rise is inductively limited, τ_a contains a contribution from the geometrical inductance, the baffle geometry, and the holdoff voltage. To normalize the effects of these contributions, a dimensionless switching time, τ_r is defined as

$$\tau_r = \frac{\tau_a}{\left[\Delta I / \left(\frac{dI}{dt}\right)_L\right]} = \frac{\tau_a V_A}{L_g \Delta I}, \quad \left(\frac{dI}{dt}\right)_L = \frac{V_A}{L_g}, \qquad (8)$$

where ΔI is the specified current denoting switching, V_A is the anode holdoff voltage, L_g is the geometrical inductance, and $(dI/dt)_L$ is the inductively limited rate of current rise.

The dimensionless switching time is plotted in Fig. 11 for a selection of baffle offsets as a function of holdoff voltage ($\Delta I = 2$ kA, $L_g = 75$ nH). For these conditions τ_r increases with increasing V_A. The change in switching time for thyratrons with different baffle offsets is approximately constant for all V_A. The increase in τ_r as V_A increases is largely a result of the decrease in the inductively limited rate of current rise. The absolute switching time *does* decrease with increasing V_A, as shown in Fig. 11 for $D_b = 3$ mm. This rate of decrease, though, is smaller than the rate of decrease in switching time one would calculate based only on inductance and holdoff voltage. The normalized switching time, τ_r, therefore increases. This implies that the noninductive component to the switching time (e.g., electron avalanche and plasma spreading time) decreases only slowly with increasing V_A. The slow decrease results from tight baffling of the control grid slot. Tight baffling, a requirement for high-voltage holdoff, results in a limited amount of penetration of anode potential into the cathode-control grid gap.

VI. CONCLUDING REMARKS

A model for commutation in a thyratron has been described and the results compare favorably to experiment. The model consists of a Monte Carlo particle simulation for electrons coupled to a fluid representation for ions. Each particle represents a specified number of electrons. A weighting and renormalization technique is used to simulate electron avalanche over many orders of magnitude using a finite number of particles. By use of a modified null cross-section technique, Monte Carlo methods can be implemented while the density of electron collision partners change. The tradeoff between holdoff voltage and switching speed was examined by varying the dimensions of the control grid baffle. We found that commutation progresses through two stages; "runaway" and "collisional." The transition results from a decrease in anode and grid voltages, and a reduction in average electron energy. This reduction moves the electron swarm into a regime where the collision frequency is higher. We also found that the noninductive switching time, as measured by the rate of current rise, decreases only slowly with increasing anode voltage. This implies that the rate of electron avalanche and plasma spreading is determined largely by the grid voltages and grid geometries. Monte Carlo particle simulations, as described in this paper, are useful tools for analyzing low-pressure discharge devices having complex geometries, during transients, and when inelastic collisions are important. During the conduction phase, though, continuum methods of analysis appear to be computationally more suited.

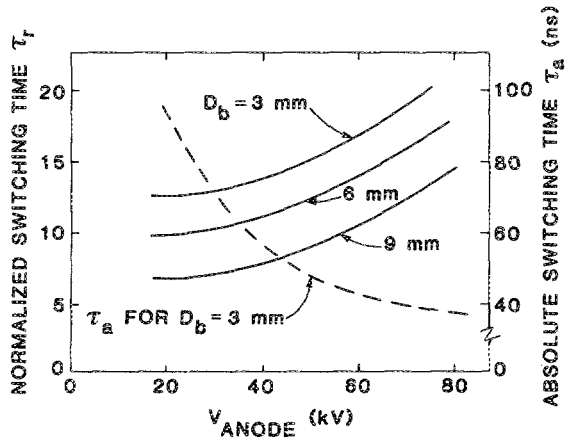

FIG. 11. Normalized switching time (solid line) as a function of anode holdoff voltage for different values of the baffle-control grid offset D_b. Also plotted is the absolute switching time (dashed line) for $D_b = 3$ mm.

ACKNOWLEDGMENTS

The author would like to thank Rodney A. Petr and Joseph S. Demboski for their assistance in obtaining the experimental results discussed in this paper. The author would also like to thank Dr. David Turnquist for building the original prototype linear thyratron.

[1] S. Goldberg, and J. Rothstein, Adv. Electron Phys. **14**, 207 (1961).
[2] D. Turnquist, R. Caristi, S. Friedman, S. Merz, R. Plante, and N. Reinhardt, IEEE Trans. Plasma Sci. **PS-8**, 185 (1980).
[3] A. Endoh, S. Watnabe, and M. Watnabe, J. Appl. Phys. **55**, 1322 (1984).
[4] B. M. Penetrante and E. E. Kunhardt, J. Appl. Phys. **59**, 3383 (1986).
[5] J. A. Kunc, and M. A. Gundersen, IEEE Trans. Plasma Sci. **PS-10**, 315 (1982).
[6] J. A. Kunc and M. A. Gundersen, Phys. Fluids **27**, 2862 (1984).
[7] D. A. Erwin, J. A. Kunc, and M. A. Gundersen, Appl. Phys. Lett. **48**, 1727 (1986).
[8] J. A. Kunc, S. Guha, and M. A. Gundersen, Laser Part. Beams **1**, 395 (1983); J. A. Kunc and M. A. Gundersen, Laser Part. Beams **1**, 407 (1983).
[9] R. A. Petr, M. J. Kushner, S. R. Byron, C. H. Fisher, J. J. Ewing, and D. Turnquist, *Proceedings of the 5th IEEE Pulsed Power Conference, Arlington, VA, 1985* (IEEE, New York, 1985), pp. 227–230.
[10] M. J. Kushner, C. H. Fisher, J. Demboski, and R. A. Petr, J. Appl. Phys., **60**, 2766 (1986).
[11] L. E. Kline and J. G. Siambis, Phys. Rev. A **5**, 794 (1972).
[12] S. L. Lin and J. N. Bardsley, J. Chem. Phys. **66**, 435 (1977).
[13] M. Hayashi, "Recommended Values of Transport Cross Sections for Elastic and Total Collision Cross Section for Electrons in Atomic and Molecular Gases," Nagoya Institute of Technology, IPPJ-AM-19, 1981.
[14] W. C. Fon, K. A. Barrington, P. G. Burke, and A. E. Kingston, J. Phys. B **14**, 2921 (1981).
[15] F. G. Donaldson, M. A. Hender, and J. W. McConkey, J. Phys. B. **5**, 1482 (1972).
[16] D. Rapp and P. Englander-Golden, J. Chem. Phys. **43**, 1464 (1965).
[17] K. Stephens, H. Helm, and T. D. Mark, J. Chem. Phys. **73**, 3763 (1980).
[18] A. E. S. Green and T. Sawada, J. Atmos. Terr. Phys. **34**, 1719 (1972).

[19]L. Vriens, Phys. Lett. **8**, 260 (1964).
[20]M. Mitchner and C. H. Kruger, *Partially Ionized Gases* (Wiley, New York, 1973), pp. 54–62.
[21]G. L. Braglia, Physica **92C**, 91 (1977).
[22]J. Dutton, J. Phys. Chem. Ref. Data **4**, 577 (1975).
[23]E. L. Duman and B. L. Smirnov, High Temp. **12**, 431 (1974).
[24]H. W. Willis, R. Y. Pai, and E. W. McDaniel, At. Data Nuc. Data Tables **17**, 177 (1976).
[25]W. F. Ames, *Numerical Methods for Partial Differential Equations* (Academic, New York, 1977), pp. 119–125.
[26]C. K. Birdsall and A. B. Langdon, *Plasma Physics via Computer Simulation* (McGraw-Hill, New York, 1985), pp. 277–301.